

Bottom and top reconstruction as benchmarks for the ILD Detector

M.S. Amjad^a, A. Irles^b, V. Lohezic^c, Y. Okugawa^d, R. Pöschl^b, F. Richard^b,
H. Yamamoto^d, R. Yonamine^d

^aNational University of Technology, Islamabad, Pakistan

^bUniversité Paris-Saclay, CNRS/IN2P3, IJCLab, 91405 Orsay, France

^cUniversité Paris-Saclay, Espace Technologique Bât. Discovery - RD 128 - 2e ét., 91190 Saint-Aubin, France

^dTohoku University, 6-3 Aoba Aramaki-aza Aoba-ku, Sendai 980-8578, Japan

Abstract

A comprehensive study of bottom-quark pair and top-quark pair production using the lepton+jets channel at $\sqrt{s} = 500$ GeV is presented that benchmark the performance of the current so-called *large* and *small* models of the ILD Detector. The event reconstruction exploits features of the detector such as lepton identification, vertex charge reconstruction and particle ID with the central TPC of the ILD Detector. With these techniques the final state leptons, the b -quark and \bar{b} -quark and the W can be unambiguously reconstructed. Both detector models perform similarly well with a slight advantage of the large detector model. In case of top quark pair production the selection efficiency is between 30% and 60% for semi-leptonic events. For this channel the note presents an update of the perspective of the physics potential w.r.t. earlier studies for an integrated luminosity of 3200 fb^{-1} . The results for $e^+e^- \rightarrow b\bar{b}$ demonstrate that also this channel can accurately measured at $\sqrt{s} = 500$ GeV.

1. Introduction

Heavy quarks may be messengers of new physics of primary importance [1]. Their large mass compared with other fermions can be explained in Randall Sundrum models [2, 3] featuring warped extra dimensions that are dual to model, which assume that the heavy quarks are composite objects [4]. High precision e^+e^- collisions with polarised beams around the TeV scale, as would be available with the International Linear Collider ILC, are ideally suited to detect new physics effects [5, 6]. This note presents detailed simulation studies with the ILD detector concept [7] of the processes $e^+e^- \rightarrow t\bar{t}$ and $e^+e^- \rightarrow b\bar{b}$ at a centre-of-mass energy $\sqrt{s} = 500$ GeV. The analyses in Refs. [8, 6] carried out for the ILD detector baseline design DBD [7] are ported to the large, IDR-L, and small, IDR-S, detector models, respectively, of the ILD detector [7] for the International Linear Collider [9]. These detector models differ by the outer radius of the TPC that is the central tracking device of ILD. The model IDR-L features an outer TPC radius of 177 cm and the model IDR-S features an outer TPC radius of 143 cm.

Precise measurements of the electroweak couplings of third-generation quarks require superb detector performance in terms of flavour tagging including the event by event determination of the charge of the final state jets to avoid for example migrations in polar angle spectra and/or to reconstruct events in which the heavy quark charge is the only handle to distinguish between particles and anti-particles. The charge determination happens mainly by a combination of the determination of the summed charge of tracks pointing to a secondary vertex (Method labeled Vtx hereafter) or by the identification of the charge of a final state Kaon (Method labeled K hereafter). The latter method requires a successful particle identification by the detector. Therefore processes with heavy quark final states are highly relevant for the benchmarking of the detector performance. In this note we will use the $e^+e^- \rightarrow b\bar{b}$ and $e^+e^- \rightarrow t\bar{t}$ final states to benchmark the tracking and vertexing capabilities of the

ILD tracking system and the charged particle ID performance of the TPC. The results here benefit from a refined analysis strategy for the $e^+e^- \rightarrow b\bar{b}$ process. A more complete account of this analysis strategy will be published in Ref. [10].

2. Methods, tools and Monte Carlo samples

For the event reconstruction we use the `ILCSOFT` version v02-00-02. The software allows for a full detector simulation and event reconstruction including digitisation steps. We use the versions `ILD_s5_o1_v02` and `ILD_15_o1_v02` of the detector model.

For the event reconstruction we use the following methods

- ‘Core tools’

- We use the standard `LeptonFinder` of ILD to identify isolated electrons and muons in semi-leptonic $t\bar{t}$ events.
- In case of $e^+e^- \rightarrow t\bar{t}$ we use the generalised k_t algorithm for e^+e^- collisions as implemented in the `FastJet` package [11].

In this algorithm the distance between two objects is calculated as

$$d_{ij} = \min(E_i^{2\beta}, E_j^{2\beta})(1 - \cos \theta_{ij}) / (1 - \cos R) \quad (1)$$

The distance of a particle i to the beam is calculated according to.

$$d_{iB} = E_i^{2\beta} \quad (2)$$

The latter allows for removing background from $\gamma\gamma$ -collisions.

The jet algorithm is run with the following settings: $\beta = 1$ and $R = 1.5$.

- We use the `LCFIPlus` package [12] for vertex finding, the association of the vertices with jets and flavour tagging.
- In case of $e^+e^- \rightarrow b\bar{b}$ we use the Valencia jet algorithm implemented in `LCFIPlus` [13]. In this algorithm the distance between two objects is calculated as

$$d_{ij} = 2 \min(E_i^{2\beta}, E_j^{2\beta})(1 - \cos \theta_{ij}) / R^2 \quad (3)$$

The distance of a particle i to the beam is calculated according to.

$$d_{iB} = E^{2\beta} \sin^{2\gamma} \theta_{iB} \quad (4)$$

The jet algorithm is run with the following settings: $\alpha = \beta = \gamma = 1$, $R = 1.4$

We apply the option in which tracks belonging to a secondary vertex are replaced by one B-hadron avoiding thus breaking of secondary vertices.

- Tools developed for the study

- We identify reconstructed tracks that have not been associated to secondary vertices from B-Meson decays but belongs to this decay according to the Monte Carlo Truth information. Based on this knowledge the algorithm described in Ref. [6] recovers the ‘lost’ tracks by means of the impact parameters d_0 (transversal) and z_0 (longitudinal), information that would be available from detector signals. In this present note the recovery uses only the impact parameter d_0 since the algorithms needs to be adapted for the vertex smearing present in the simulation for the IDR.

- We identify charged Kaons by means of the dE/dx measured in the TPC of ILD. The particle ID algorithm selects a strip in the dE/dx -momentum plane with a high kaon concentration. The efficiency and the purity of the Kaon selection vary as a function of the width of this strip.
- We finally calculate the jet charge and the polar angle of the bottom and top quark pair, respectively.

The following method combines the results of the two (nearly independent) charge measurements on the b and \bar{b} jet into a robust charge determination.

$$\left. \begin{aligned} N_{acc} &= Np^2 + Nq^2 \\ N_{rej} &= 2Npq \\ 1 &= p + q \end{aligned} \right\} N_{corr} = N_{acc} \cdot \frac{p^2}{p^2 + q^2} \quad (5)$$

where N is total number of events, N_{acc} and N_{rej} are the number of events that were accepted and rejected, respectively. The p and q values represent the probabilities for a correct or an incorrect reconstruction of the b quark charge, respectively. The correction has been applied to the $b\bar{b}$ studies but not (yet) for $t\bar{t}$. For the latter the selection scheme in $t\bar{t}$ is more involved rendering its application less straight forward since e.g. the b quarks are not necessarily back-to-back.

2.1. Monte Carlo samples

The signal samples were generated with WHIZARD 1.95. Top quark pair production is the dominant process in the $e^+e^- \rightarrow b\bar{b}\ell\nu q\bar{q}$ sample, but it contains also single t and WWZ . In case of the t quark study we have analysed samples for the beam polarisations $\mathcal{P}_{e^-}, \mathcal{P}_{e^+} = \pm 1, \mp 1$. In total we analyse about 2200 fb^{-1} for each of the beam polarisations but we discard final states for which $W \rightarrow \tau\nu$. In case of the b quark study we have studied only the configuration $\mathcal{P}_{e^-}, \mathcal{P}_{e^+} = -1, +1$ since this study is just considered as a supporting study for the t quark analysis and the chosen polarisation configuration is the more challenging for the detector performance due to larger migration effects in the polar angle reconstruction. The $b\bar{b}$ events are extracted from a sample of simulated $q\bar{q}$. The total integrated luminosity is about 46 fb^{-1} . The genuine $e^+e^- \rightarrow b\bar{b}$ at 500 GeV is about 4% of the total cross section.

The control plots in Secs. 3 and 4.2 are given for the process $e_L^- e_R^+ \rightarrow t\bar{t}$ in this note.

3. Efficiencies and Control plots

Figure 1 demonstrates that the studies presented in this note test the detector performance for very different momenta of the final state b quark.

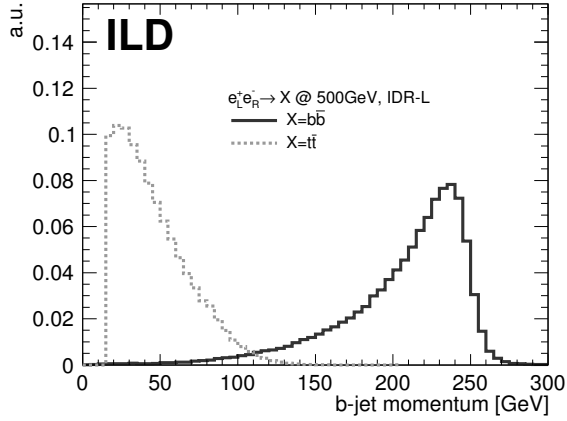


Figure 1: Momentum of the b -jet with cheated identification for $e_L^- e_R^+ \rightarrow b\bar{b}$ and $e_L^- e_R^+ \rightarrow t\bar{t}$ processes.

Figs. 2 and 3 show the number of charged particles that is not associated correctly to the secondary vertex as a function of the jet polar angle, normalized to the number of reconstructed tracks and broken down by cause. Before the vertex recovery the fraction of missed charged particles is approximately 2 – 3.5‰ for jets in the central detector, dominated by particles reconstructed with a low impact parameter significance and a variety of other reasons. In the forward region the number of missed tracks increases rapidly due to the limited acceptance. Beyond a peak is visible in particular in Fig. 3 around $|\cos\theta| = 0.8$ that corresponds to the transition region between the barrel and the endcap of ILD. After the vertex recovery the fraction of missed charged particles is reduced to a level of 2 – 2.5‰ and the peak in the transition region is removed. Figure 3 demonstrates also a visible improvement in the forward region. The results are shown for the large model but are similar for the small detector model.

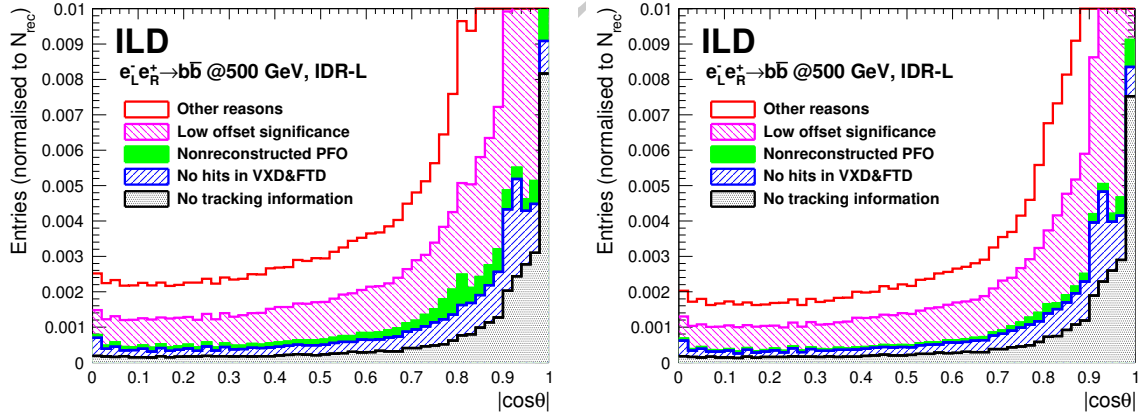


Figure 2: Fraction of missed tracks created by charged particles as a function of the polar angle of the generated particles before (left) and after (right) vertex recovery in case of the $e_L^- e_R^+ \rightarrow b\bar{b}$ process.

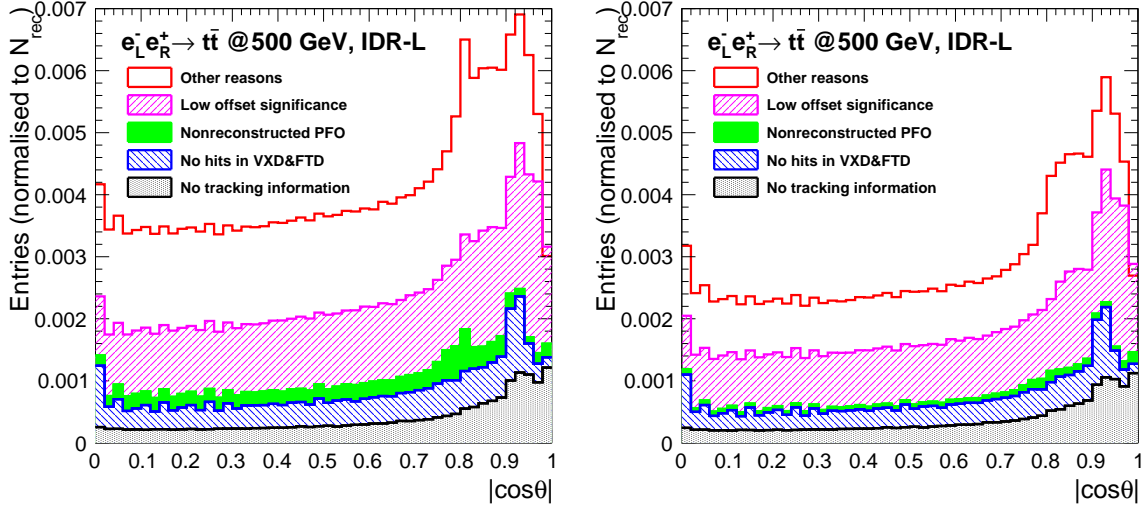


Figure 3: Fraction of missed tracks created by charged particles as a function of the polar angle of the generated particles before (left) and after (right) vertex recovery in case of the $e_L^- e_R^+ \rightarrow t\bar{t}$ process.

This improvement is quantified in Figs. 4 and 5 where the purity of the b -charge reconstruction is shown as a function of the b -tag value, the reconstructed b -momentum $|p_{B,had}|$, the number of reconstructed tracks assigned to a secondary vertex N_{rec} and finally the polar angle of the b -hadron. here denoted as $|\cos \theta|$. The b -charge Purity is defined as

$$P_b = N_{correct}/N_{jet,tot}. \quad (6)$$

with $N_{correct}$ being the number of b -jets with correctly reconstructed b quark charge. This value normalised to the total number of b -jets $N_{b-jet,tot.}$ for which a charge assignment according to e.g. Table 2 can be made.

The improvement is larger for the process $e_L^- e_R^+ \rightarrow t\bar{t}$ than for $e_L^- e_R^+ \rightarrow b\bar{b}$. Qualitatively this is expected since as a consequence of the different b -jet momenta, see Fig. 1, also the tracks produced in the decay of the b -hadron are softer in case of top-pair production. In case of $e^+ e^- \rightarrow t\bar{t}$ the improvement is 10% over a large range in $|\cos \theta|$ and mainly driven by three to five prong decays. Both results will further improve once the vertex recovery takes also the impact parameter z_0 into account. All results shown so far in this section have been obtained for the large detector model. The conclusions for the small detector model are similar.

The lower right panels of Figs. 5 and 4 show a drop in purity for large values of $|\cos \theta|$. This is compatible with the drop in efficiency shown in Fig. 6 for the case $e_L^- e_R^+ \rightarrow b\bar{b}$ as a function of the polar angle of the reconstructed b -jet $|\cos \theta_b|$. Within statistical errors the results are the same for the large and the small detector model. However, towards large values of $|\cos \theta_b|$ the efficiency observed for the large detector is systematically above that of the small detector.

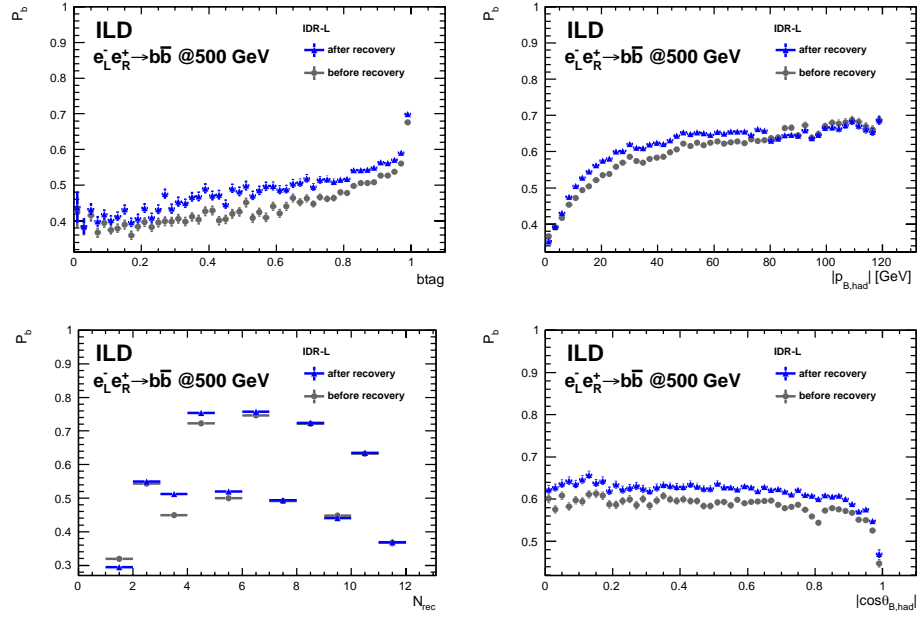


Figure 4: Purity before and after vertex recovery in case of the $e_L^- e_R^+ \rightarrow b\bar{b}$ process for different observables.

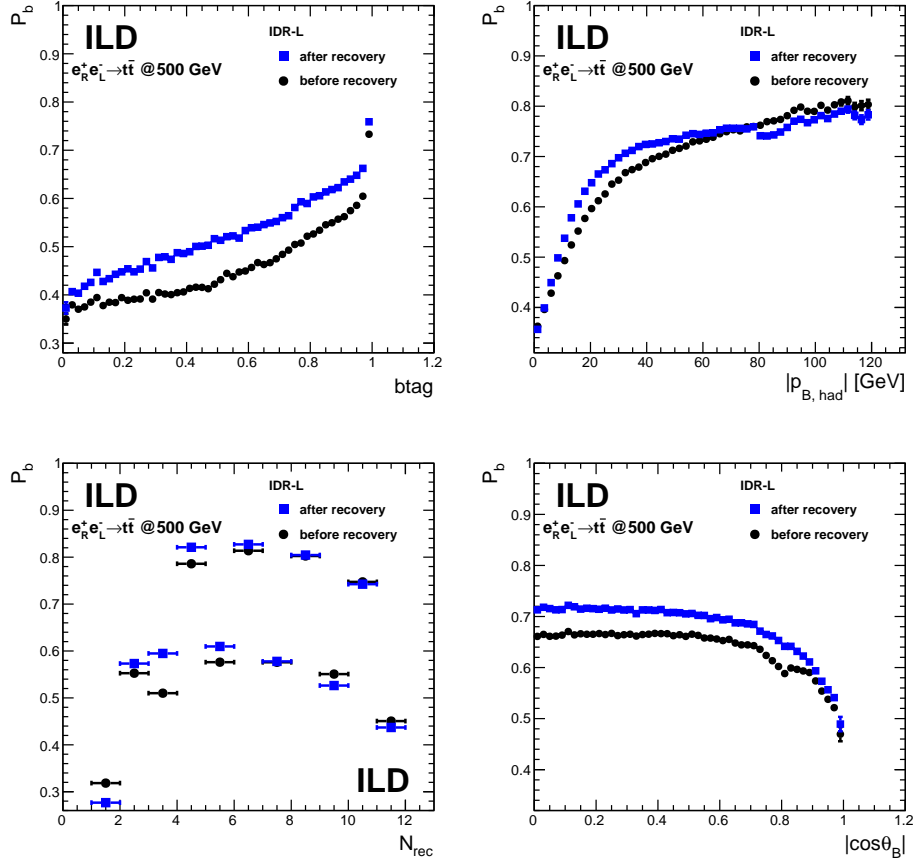


Figure 5: Purity before and after vertex recovery in case of the $e_L^- e_R^+ \rightarrow t\bar{t}$ process for different observables.

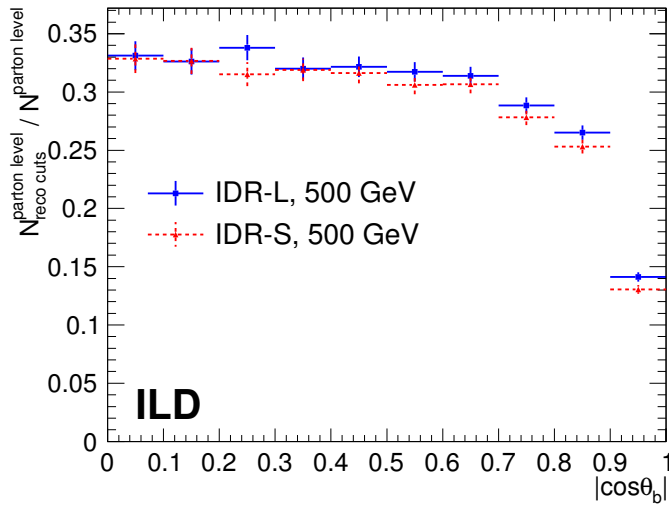


Figure 6: Reconstruction efficiency for b-tagged jets. Note the figure shows the efficiency after the full selection given in Tab. 1.

A component that distinguishes the ILD Detector from other proposals for e^+e^- colliders is the TPC as the central tracking system. Beside the precise momentum measurement the dE/dx measurement in the gaseous medium allows for a particle identification. Since around 87% of B-Mesons (neutral or charged) contain a charged Kaon among their decay products the particle ID can support greatly the charge determination of the b quark.

The left part of Fig. 7 shows the dE/dx values obtained in simulation for different particle types as a function of the particle momentum. The lines indicate a strip with an accumulation of signals produced by Kaons. A minimum momentum of 2 GeV is required for the selection of Kaons. The right part of Fig. 7 shows the variation of the purity as a function of the Kaon selection efficiency that corresponds to a variation of the width of the strip in the previous figure. In general the efficiency is higher for $e_L^- e_R^+ \rightarrow t\bar{t}$ than for $e_L^- e_R^+ \rightarrow b\bar{b}$. This is expected since b-jets issue of the t quark is softer than the b-jets in case of $e_L^- e_R^+ \rightarrow b\bar{b}$. Moreover, the efficiency obtained for IDR-L is on average higher than for IDR-R. At least qualitatively this can be explained by the on average longer tracks in case IDR-L that yield a better dE/dx resolution. A closer look into the separation power in different momentum ranges is given in App. A.

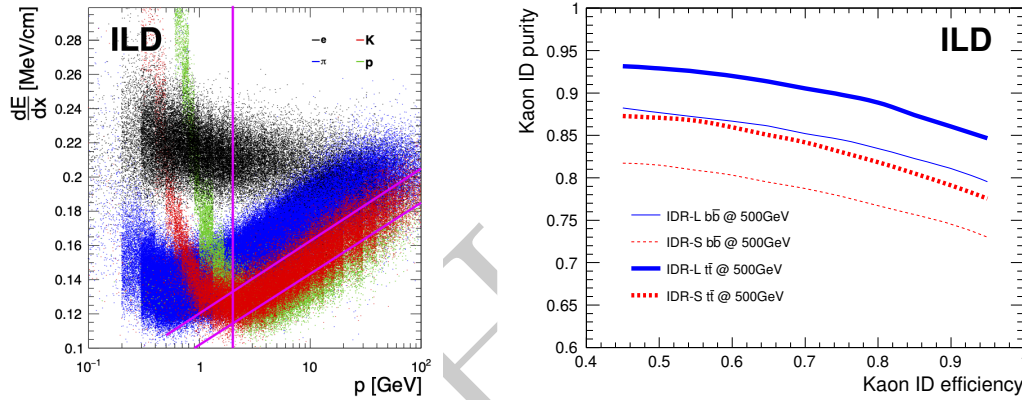


Figure 7: Left: Simulated dE/dx spectrum for different particle types. The lines indicate the cuts for the Kaon selection. Right: Purity of the Kaon selection as a function of the Kaon selection efficiency.

4. Event selection

In the following the event selection of the two final states under study will be presented. The different complexities of the final states require different set of cuts. The t quark is composed from its decay products, the b quark and the W boson and the final state lepton.

4.1. Analysis details specific to the $e_L^- e_R^+ \rightarrow b\bar{b}$ analysis

Table 1 shows the selection efficiencies for the $e_L^- e_R^+ \rightarrow b\bar{b}$ analysis. In this case events that are subject to the radiative return to the Z , implying an energetic final state photon, have to be suppressed. Therefore cuts on the sum of the masses of the two jets and a cut on the photon energy are introduced. The overall efficiency after selection of events with consistent b quark charge is with around 28% to 29% similar for both detector models. For the b -charge measurement opposite charges in opposite jets are required. The charges are either derived from the tracks pointing to the secondary vertex or from the Kaon charge or from a combination of both. An event is selected if there is one combination with a consistent result. The efficiencies for the different methods are given in Tab. 2. The purity of the different methods is shown in Fig. 8. In both cases there is no large difference between the two detector models although the large detector seems to perform slightly better for the double Kaon method, in agreement with the observations in the right part of Fig. 7.

$$e_L^- e_R^+ \rightarrow b\bar{b} \text{ at } 500 \text{ GeV}$$

	IDR-L			IDR-S		
	Signal	B _{q\bar{q}} /S	B _{rad.Z} /S	Signal	B _{q\bar{q}} /S	B _{rad.Z} /S
Full sample	100.0%	1800.5%	359.1%	100.0%	1800.6%	359.0%
$b_{tag}(jet_1) > 0.9$ and $b_{tag}(jet_2) > 0.2$	70.2%	2.3%	147.7%	69.9%	2.3%	149.0%
$m_{jet_1+jet_2} > 200 GeV$	68.2%	1.4%	6.7%	67.8%	1.2%	6.7%
$E_{photon} < 100 GeV$	64.8%	1.3%	1.7%	64.3%	1.2%	1.6%
double jet-charge measurement	28.9%	1.0%	1.0%	27.9%	0.9%	1.0%

Table 1: Selection efficiency and B/S rejection for some background sources

$$e_L^- e_R^+ \rightarrow b\bar{b} \text{ at } 500 \text{ GeV}$$

	IDR-L	IDR-S
$Vtx+Vtx$	12.9%	12.8%
$K+K$	4.4%	4.0%
$Vtx+K$ (diff. jets)	3.9%	3.7%
$Vtx+K$ (same jet)	7.7%	7.4%

Table 2: Final selection efficiency, after double jet-charge measurement

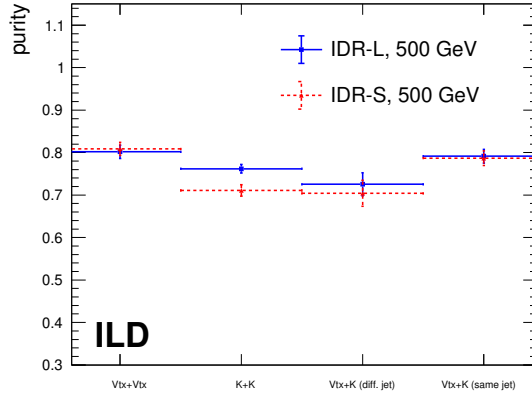


Figure 8: Purity of the methods listed in Tab. 2 used for the reconstruction of the vertex charge in the $e_L^- e_R^+ \rightarrow b\bar{b}$.

4.2. Analysis details specific to the $e_L^- e_R^+ \rightarrow t\bar{t}$ analysis

The t quark is composed from its decay products, the b quark and the W boson and the charge of the lepton is a measure to distinguish the t from the \bar{t} quark.

Figure 9 shows in the left panel the energy distribution of the isolated lepton in the laboratory frame. The distribution features a maximum at around 30 GeV and a tail towards higher energies. The right panel shows the polar angle spectrum of the isolated lepton. The distribution decreases slightly with a sharp drop at the acceptance limit of the detector. The distribution reveals also acceptance drops at $\cos\theta_\ell = 0$ and $\cos\theta_\ell = 0.8$ that correspond to the position of the TPC anode plate and the barrel-endcap transition region, respectively.

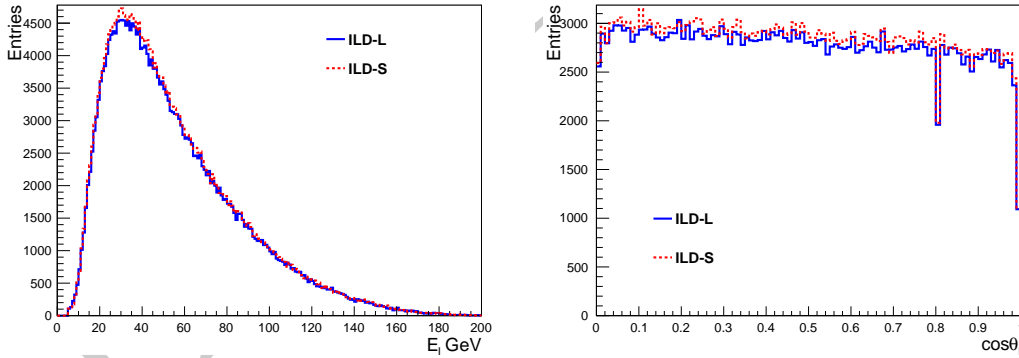


Figure 9: Left: Energy of the isolated lepton in $e_L^- e_R^+ \rightarrow t\bar{t}$. Right: Polar angle distribution of the isolated lepton in $e_L^- e_R^+ \rightarrow t\bar{t}$.

For completeness Fig. 10 shows the mass distribution of the hadronic W and the hadronic t quark.

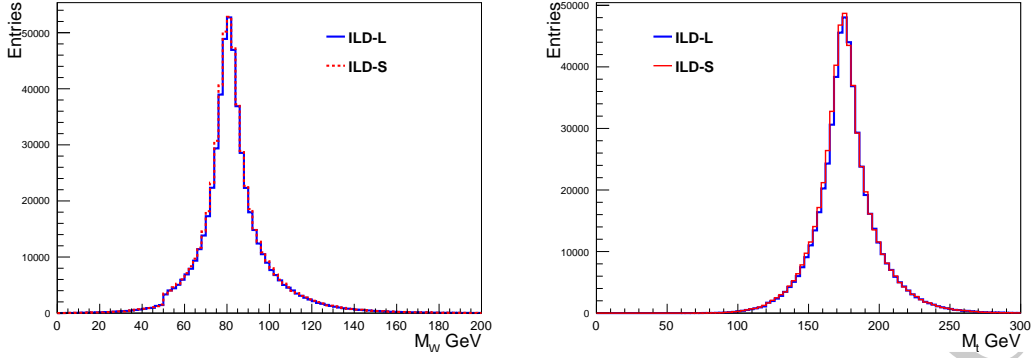


Figure 10: Left: Mass distribution of the hadronic W in $e_L^- e_R^+ \rightarrow t\bar{t}$. Right: Mass distribution of the hadronic t quark in $e_L^- e_R^+ \rightarrow t\bar{t}$.

Tables 3 and 5 give the efficiencies after each cut applied for the selection of $t\bar{t}$ events. The first part lists *General selection cuts* that were already used in Ref. [5].

The polar angle of the t quark $\cos\theta_t$ is reconstructed from the hadronically decaying t quark. For the polar angle spectrum the charge of the t quark has to be determined and the b quark and the W -boson have to be correctly associated. This is more involved in the $e_L^- e_R^+ \rightarrow t\bar{t}$ case than in the $e_R^- e_L^+ \rightarrow t\bar{t}$ case due to the different kinematics provoked by the $V - A$ interaction of the t quark decay. The different steps for an accurate reconstruction of the polar angle spectrum are listed in the following¹.

- In a first step further cuts on the sum of the Lorentz factor of the two tops of $\gamma_t^{had} + \gamma_t^\ell > 2.4$ is applied. Here γ_t^{had} is the Lorentz factor of the hadronically decaying t quark and γ_t^ℓ the Lorentz factor of the leptonically decaying t quark. In case of $e_L^- e_R^+ \rightarrow t\bar{t}$ a cut on the B -hadron momentum of $p_{B,had.} > 15$ GeV is applied in addition.
- The semi-leptonic decay of the t quark gives powerful information for the event reconstruction giving rise to the variable L_{cut} , which means the charge of the isolated lepton plus a cut on the event quality of $\chi^2 < 15$ that is motivated in Ref. [5].
- For the b quark charge determination the used methods are very much similar to those in 2. The vertex charge is supported by the requirements of $btag > 0.8$ and a minimal hadron momentum of 25 GeV as motivated in Ref. [6]².
- The various methods of measuring the b quark charge are also combined with the charge of the isolated lepton L . In this case an additional cut on $\gamma_t^{had} > 1.23$ is applied.
- The final decision on the t quark charge is obtained from the sum of the charges associated to the different methods. If the sum is smaller (greater) than zero then the hadronically decaying t quark candidate is said to be the t quark (\bar{t} quark).

Table 3 gives the final selection efficiency for the case $e_L^- e_R^+ \rightarrow t\bar{t}$ after the inclusion of the respective cuts. Table 4 shows the *accumulated* efficiencies for $t\bar{t}$ identification after progressive application of the various methods described in the list of items above. The addition of methods other than that based on the lepton charge only (‘Method 1’ in Tab. 4) increases the efficiency by around 38%. Figure 11

¹We are aware that the set of cuts does not look straight forward and needs revision in the Post-IDR phase.

²In the $e^+e^- \rightarrow b\bar{b}$ analysis this additional requirement was removed. It would have to be investigated whether this requirement can be omitted in case of $e_L^- e_R^+ \rightarrow t\bar{t}$, too

$e_L^- e_R^+ \rightarrow t\bar{t}$ at 500 GeV

General selection cuts	IDR-L	IDR-S
Isolated Lepton	92.1%	92.1%
$btag_1 > 0.8$ or $btag_2 > 0.3$	81.2%	81.1%
Thrust < 0.9	81.2%	81.1%
Hadronic mass	78.2%	78.2%
Reconstructed m_W and m_t	73.4%	73.4%
t quark polar angle spectrum		
$\gamma_t^{had.} + \gamma_t^\ell > 2.4$	62.2%	61.8%
$ p_{B,had} > 15$ GeV	34.5%	33.9%
" $t\bar{t}$ identification"	30.6%	30.2%
b quark polar angle spectrum		
No additional cuts		

Table 3: Event selection efficiencies after pre-selection and reconstruction of the polar angle spectrum of the t quark and that of the underlying b quark for the process $e_L^- e_R^+ \rightarrow t\bar{t}$.

Methods	IDR-L	IDR-S
1 L_{cut}	22.1%	21.9%
2 $L+Vtx$	28.6%	28.4%
3 $L+K$	29.6%	29.3%
4 $Vtx+Vtx$	30.1%	29.7%
5 $K+K$	30.3%	29.9%
6 $Vtx+K$ (same jet)	30.5%	30.1%
7 $Vtx+K$ (different jet)	30.6%	30.2%

Table 4: Efficiency increase after the progressive application of the various methods introduced to ensure a correct association of the W boson and the b quark in case of $e_L^- e_R^+ \rightarrow t\bar{t}$. The final efficiency in the last line of this table corresponds to the efficiency given in the line " $t\bar{t}$ identification" of Tab. 3.

shows for completeness the purity of the selection for those cases in which the information from the t quark and the \bar{t} quark decay have been combined. As in case of $e_L^- e_R^+ \rightarrow b\bar{b}$ differences between the large and the small detector are observed for those combinations that include Kaons with the biggest difference for the pure Kaon combination $K + K$. The Kaon measurement is the domain of the TPC and the two models feature different outer TPC radii.

As a supplementary remark please note that methods available also for the fully hadronic final state yield efficiencies of 14.4% when using Methods 4-7 of Tab. 4 and 6.9% when using only Method 4, respectively.

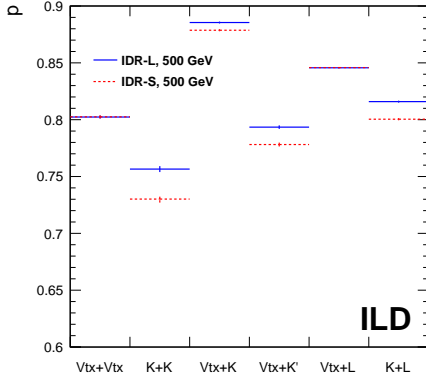


Figure 11: Purities of the various combinations

$e_R^- e_L^+ \rightarrow t\bar{t}$ at 500 GeV		
General selection cuts	IDR-L	IDR-S
Isolated Lepton	94.1%	94.0%
$btag_1 > 0.8$ or $btag_2 > 0.3$	84.9%	84.8%
Thrust < 0.9	84.9%	84.8%
Hadronic mass	82.2%	82.3%
Reconstructed m_W and m_t	77.6%	77.5%
t quark polar angle spectrum		
$\gamma_t^{had.} + \gamma_t^\ell > 2.4$	64.1%	64.1%
b quark polar angle spectrum		
$Vtx+Vtx$	10.8%	10.3%

Table 5: Event selection efficiencies after pre-selection and reconstruction of the polar angle spectrum of the t quark and that of the underlying b for the process $e_R^- e_L^+ \rightarrow t\bar{t}$

Table 5 shows the selection efficiencies for the case $e_R^- e_L^+ \rightarrow t\bar{t}$. The cut scenario for the reconstruction of the polar angle of the t quark is much simpler than in case of $e_L^- e_R^+ \rightarrow t\bar{t}$. The reason is that the t quark direction is in first approach given by the W boson such that a wrong association of W boson and b quark doesn't alter the t quark direction. For the polar angle spectrum of the underlying b quark the analysis is restricted to the the combination of the vertex charge. This is further discussed in Sec. 5.

5. Results

Figure 12 shows the spectrum of the polar angle $\cos \theta_b$ after the selection given in Tabs. 1 and 2 and the application of Eq. 5 for $e_L^- e_R^+ \rightarrow b\bar{b}$. Large and small detector agree within statistical uncertainties.

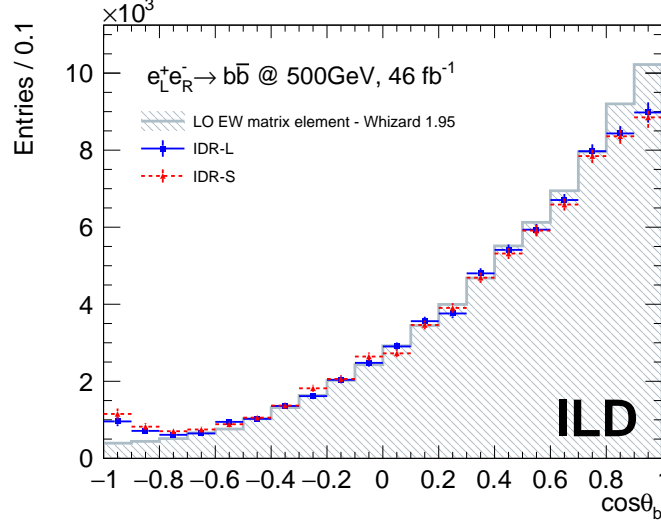


Figure 12: Polar angle spectrum for $e_L^- e_R^+ \rightarrow b\bar{b}$ at $\sqrt{s} = 500$ GeV after correction for acceptance and migrations due to charge mismeasurement, see Eq. 5, for the two ILD Detector models.

The left part of Fig. 13 shows the polar angle distribution of $t\bar{t}$ of the generated and reconstructed data for the large and the small detector models. For this all cuts and methods given in Tabs. 3 and 4 have been applied. Overlaid and here and in the following figures, mainly to guide the eye, is a polynomial of second degree motivated by the approximate $d\sigma/d\cos\theta_t \sim S\cos^2\theta_t + A\cos\theta_t$ dependence of the differential cross section. The right part shows the polar angle distribution of the underlying b quark for the same set of cuts. The polar spectrum can be accurately reconstructed over the entire polar angle. Acceptance drops at large absolute values of the polar angle become visible in the polar angle spectrum of the b quark (In this case no attempt was made to correct for acceptance as in Fig. 12). However, in the range $-0.8 < \cos\theta_b < 0.8$ also the polar angle of the b quark can be accurately reconstructed.

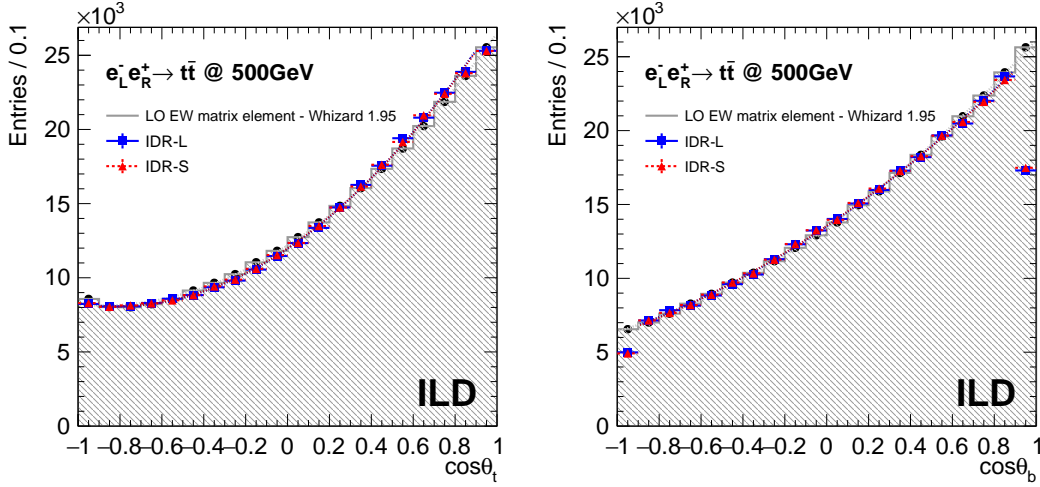


Figure 13: Results for $e_L^- e_R^+ \rightarrow t\bar{t}$ at $\sqrt{s} = 500$ GeV for the two ILD Detector models. *Left:* Polar angle distribution for t quark. *Right:* Polar angle distribution for the b quark that is issue of the t quark decay. The distributions for IDR-S is normalised to the one for IDR-L so that both histograms will be on the same level. For details on the selection, see text and Tabs. 3 and 4.

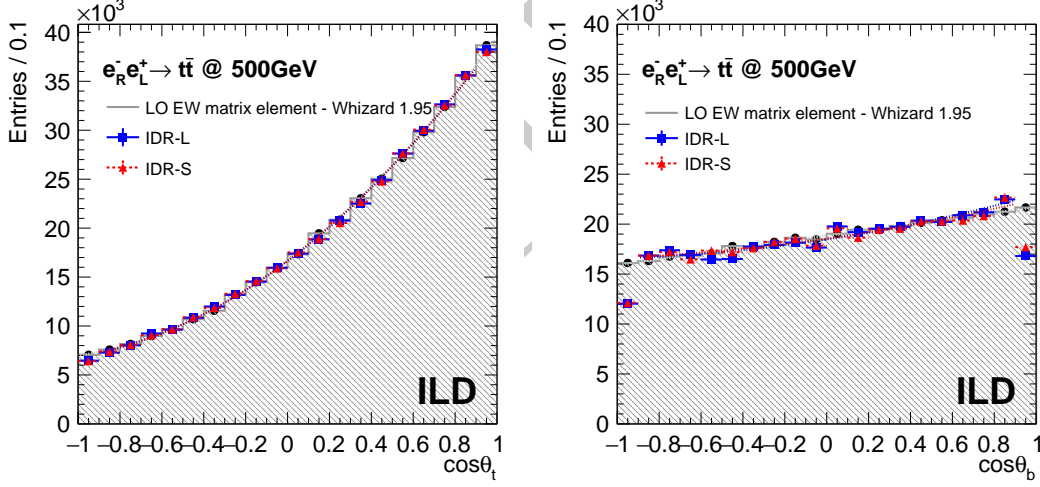


Figure 14: Same as Fig. 13 for $e_R^- e_L^+ \rightarrow t\bar{t}$. For details on the selection, see text and Tab. 5.

The left part of Fig. 14 shows the polar angle spectrum for the case $e_R^- e_L^+ \rightarrow t\bar{t}$ after application of the cuts introduced in Tab. 5. The generated spectrum can be very precisely reconstructed. The right hand part of Fig. 14 shows the polar angle spectrum of the underlying b quark. Here only events with consistent vertex-charge measurements have been included. The polar angle of the b quark can also in this case be very well reconstructed. However, the efficiency drops to 10% as already quantified in the lower part of Tab. 5. The inclusion of the other methods is subject to further studies.

Comparing the spectra of the underlying b quarks demonstrates more clearly than the actual t quark polar angle spectra the different polarisations of the t quarks projected out by the flight direction of the b quark. In case of $e_L^- e_R^+ \rightarrow t\bar{t}$ the final state is enriched with left-handed t quarks. In this case the b quark is preferably emitted in the direction of the t quark. Therefore the two polar angle spectra in Fig. 13 look similar to each other. In case of $e_R^- e_L^+ \rightarrow t\bar{t}$ the final state is enriched with right-handed

240 t quarks. In this case the b quark is preferably emitted opposite to the direction of the t -quark. The
 241 polar angle of the b quark is a consequence of the Jacobian peak in the vicinity of $\cos \theta_{Wb} = 0$, with
 242 $\cos \theta_{Wb}$ being the opening angle between the b quark and the W boson, generated by the boost of
 243 the back-to-back configuration in the centre-of-mass frame of the decaying t quark into the laboratory
 244 frame.

245 5.1. Interpretation of the results

246 Table 6 lists the generated and reconstructed value of the forward-backward asymmetry $A_{FB, reco}^t$
 247 as an estimator for the quality of the reconstruction.

	$e_L^- e_R^+ \rightarrow t\bar{t}$		$e_R^- e_L^+ \rightarrow t\bar{t}$	
	IDR-L	IDR-S	IDR-L	IDR-S
$A_{FB, gen}^t$	0.329		0.430	
$A_{FB, reco}^t$	0.342	0.340	0.430	0.430

Table 6: Selection efficiencies and resulting $A_{FB, reco}^t$ for both beam polarisations and the two detector models under study.

248 So far the results have been presented for full beam polarisation. Using the known formula [14]

$$\sigma_{\mathcal{P}_{e-}, \mathcal{P}_{e+}} = \frac{1}{4} [(1 - \mathcal{P}_{e-} \mathcal{P}_{e+})(\sigma_{-,+} + \sigma_{+,-}) + (\mathcal{P}_{e-} - \mathcal{P}_{e+})(\sigma_{+,-} - \sigma_{-,+})], \quad (7)$$

249 with $\sigma_{-,+}$ and $\sigma_{+,-}$ being the fully polarised cross-sections, the results can be extrapolated to the
 250 realistic beam polarisations of $\mathcal{P}_{e-}, \mathcal{P}_{e+} = \mp 0.8, \pm 0.3$. The resulting Born level cross sections are
 251 1070 fb in case of $\mathcal{P}_{e-}, \mathcal{P}_{e+} = -0.8, +0.3$ and 519 fb in case of $\mathcal{P}_{e-}, \mathcal{P}_{e+} = +0.8, -0.3$. The resulting
 252 statistical errors for an integrated luminosity of $\mathcal{L} = 1600 \text{ fb}^{-1}$ at each of the two polarisation settings
 253 are given in Table 7.

	$\mathcal{P}_{e-}, \mathcal{P}_{e+}$	$(\delta\sigma/\sigma)_{stat.} [\%]$	$(\delta A_{FB}^t/A_{FB}^t)_{stat.} [\%]$
IDR-L	-0.8, +0.3	0.17	0.7
	+0.8, -0.3	0.25	0.53
IDR-S	-0.8, +0.3	0.17	0.7
	+0.8, -0.3	0.25	0.53

Table 7: Statistical precisions expected for the cross sections and A_{FB}^t for the case $\mathcal{P}_{e-}, \mathcal{P}_{e+} = -0.8, +0.3$ and the two detector models under study.

254 For both, the cross section and the forward backward asymmetry it can be expected that even at
 255 full luminosity the statistical error has to be taken into account. However, the systematic errors need
 256 to be carefully estimated. For the present analysis it would have to be checked how much the sample
 257 is contaminated by events for which the semi-leptonic decay yields τ -leptons or the τ -leptons are taken
 258 into account as in [5]. The contamination by fully hadronic $t\bar{t}$ events can be expected to be small.

259 To put the results into context, the precisions on the cross-sections and the forward-backward
 260 asymmetries are translated into precisions on electromagnetic form factors of the t quark. Figure 15
 261 shows the precisions at the 1σ level expected at ILC500. The precisions are compared with those
 262 expected after the full HL-LHC running and estimations produced for FCC-ee [15] at the same confi-
 263 dence level. For ILC500, the two sets F_1 and F_2 have been extracted separately but within each set
 264 the uncertainties have been extracted simultaneously. The projections for HL-LHC are derived from
 265 the *individual* constraints of EFT Wilson coefficients presented in Tab.C2.3 of Ref. [16] (the most
 266 favourable scenario for HL-LHC). These figures demonstrate clearly the superiority of a linear e^+e^-
 267 collider with polarised beams operated at an adequate centre-of-mass energy.

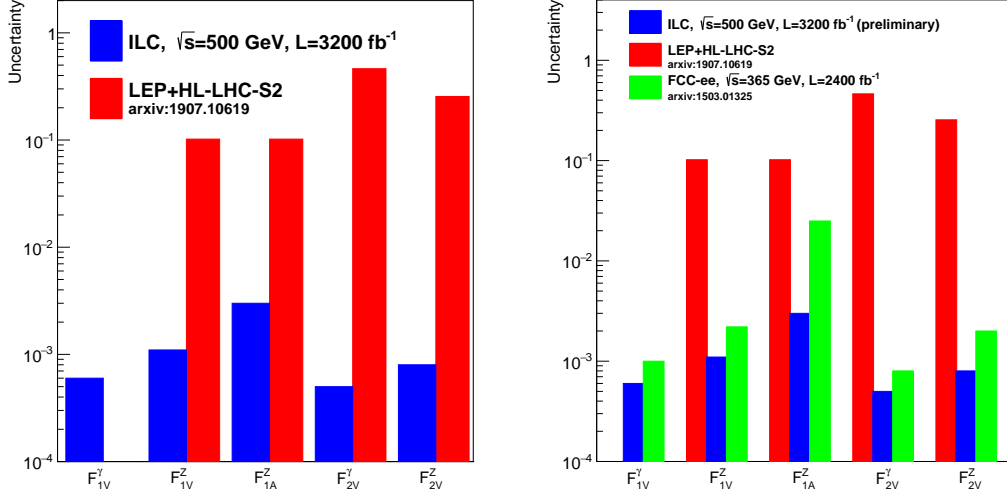


Figure 15: Precisions the on electromagnetic t quark form factors expected after ILC500 compared with those expected after the full HL-LHC running and an estimation for FCC-ee after 5000 fb⁻¹. The EFT does not include operators that map onto the F_{1V}^γ form factor. See text for further details.

6. Summary

This note presents a study of the processes $e^+e^- \rightarrow t\bar{t}$ and $e^+e^- \rightarrow b\bar{b}$ with polarised beams at $\sqrt{s} = 500$ GeV. The events are simulated and reconstructed with the large and the small models of the ILD detector.

In case of t quark pair production the analysis focuses on the semi-leptonic decay channel in which the isolated lepton is available for the distinction between the t quark and the \bar{t} quark. In case of the $e^+e^- \rightarrow b\bar{b}$ process the distinction has to be made by the measurement of the b quark charge, which helps also for a proper reconstruction of the $t\bar{t}$ quark pair. The charge of the b quark can be reconstructed with a purity of 80% using the combination of information available from the vertex charge, Kaons that have been measured in the TPC of ILD or isolated leptons in case of t -quark production.

The analysis shows that both, the large and the small detector model, are capable to provide a high precision measurement of the cross-section and the polar angle spectrum of semi-leptonic $t\bar{t}$ events with a mild advantage for the large detector. Assuming a total integrated luminosity of $\mathcal{L} = 3200 \text{ fb}^{-1}$ shared equally between the beam polarisations $\mathcal{P}_{e^-}, \mathcal{P}_{e^+} = \mp 0.8, \pm 0.3$, the cross sections of $t\bar{t}$ production can be measured to a statistical precision of about 0.2% and the forward backward asymmetry to a statistical precision of around 0.6%. The statistical precision on the cross section and the forward backward asymmetries are compatible with the scaling of the results found in [5].

For the first time the polar angle spectrum of the underlying b quark, issue of the t quark decay, is presented. This spectrum reveals more clearly the acceptance drop towards large polar angles. Still the polar angle of the b quark can be reconstructed accurately within $|\cos\theta| < 0.8$ for the two studied beam polarisations $\mathcal{P}_{e^-}, \mathcal{P}_{e^+} = \pm 1, \mp 1$. In case $\mathcal{P}_{e^-}, \mathcal{P}_{e^+} = +1, -1$ the efficiency drops however to 10% (compared with 30% for the case $\mathcal{P}_{e^-}, \mathcal{P}_{e^+} = +1, -1$). since only the vertex charge is used for this measurement. Here further work is clearly needed to improve the event yield. Both results allow however already now for the perspective that in the future the fully hadronic final state can be taken into account for the analysis and that observables specific to the produced b quark can be addressed.

The study of the $t\bar{t}$ production has been accompanied by the second benchmark study $e^+e^- \rightarrow b\bar{b}$. Since only 46 fb⁻¹ are available for this channel it should be rather considered as an auxiliary study.

However, it is shown that the polar angle spectrum can be very well reconstructed even for the hard b jets and that migrations can be controlled at a satisfactory level. It is therefore justified to conclude that ILD should be able to make precision measurements in this channel even at a centre-of-mass energy of 500 GeV.

Both analyses reveal a slight preference for the large detector model. This is most clearly visible in the purity of the charge measurement using Kaons, which may depend on the actual TPC radius due to the different track lengths.

Also in the future all heavy quark studies should be carried out in close cooperation with each other. As can be seen from the present study there are many common issues between the studies. In the future emphasis will be put on systematic uncertainties given e.g. by hemisphere correlations. These studies may be more involved in case of $t\bar{t}$ since in general the two b quarks are not back-to-back.

Acknowledgements

We thank the ILD software group for event generation, simulation and reconstruction development work.

References

- [1] F. Richard, “Present and future constraints on top EW couplings”, LAL-ORSAY-14-55, [arXiv:1403.2893 \[hep-ph\]](#).
- [2] L. Randall and R. Sundrum, “A Large mass hierarchy from a small extra dimension”, *Phys.Rev.Lett.* **83** (1999) 3370–3373, MIT-CTP-2860, PUPT-1860, BUHEP-99-9, [arXiv:hep-ph/9905221 \[hep-ph\]](#).
- [3] A. Djouadi, G. Moreau, and F. Richard, “Resolving the $A(FB)^{**}b$ puzzle in an extra dimensional model with an extended gauge structure”, *Nucl.Phys.* **B773** (2007) 43–64, LPT-ORSAY-06-060, LAL-ORSAY-06-144, [arXiv:hep-ph/0610173 \[hep-ph\]](#).
- [4] G. Durieux and O. Matsedonskyi, “The top-quark window on compositeness at future lepton colliders”, *JHEP* **01** (2019) 072, DESY 18-114, DESY-18-114, [arXiv:1807.10273 \[hep-ph\]](#).
- [5] M. S. Amjad *et al.*, “A precise characterisation of the top quark electro-weak vertices at the ILC”, *Eur. Phys. J.* **C75** (2015) no. 10, 512, IFIC-15-15, LAL-15-111, [arXiv:1505.06020 \[hep-ex\]](#).
- [6] S. Bilokin, R. Pöschl, and F. Richard, “Measurement of b quark EW couplings at ILC”, LAL-17-052, [arXiv:1709.04289 \[hep-ex\]](#).
- [7] T. Behnke, J. E. Brau, P. N. Burrows, J. Fuster, M. Peskin, *et al.*, “The International Linear Collider Technical Design Report - Volume 4: Detectors”, [arXiv:1306.6329 \[physics.ins-det\]](#).
- [8] S. Bilokin, *Hadronic showers in a highly granular silicon-tungsten calorimeter and production of bottom and top quarks at the ILC*. Theses, Paris Saclay, July, 2017. <https://tel.archives-ouvertes.fr/tel-01826535>.
- [9] C. Adolphsen, M. Barone, B. Barish, K. Buesser, P. Burrows, J. Carwardine, J. Clark, H. Mainaud Durand, G. Dugan, E. Elsen, *et al.*, “The International Linear Collider Technical Design Report - Volume 3.II: Accelerator Baseline Design”, [arXiv:1306.6328 \[physics.acc-ph\]](#).
- [10] S. Bilokin, A. Inles, R. Pöschl, and F. Richard, “Methods for b quark EW couplings measurements at ILC250 with 2000 fb $^{-1}$ ”, *Work in progress*.
- [11] M. Cacciari, G. P. Salam, and G. Soyez, “FastJet User Manual”, *Eur. Phys. J.* **C72** (2012) 1896, CERN-PH-TH-2011-297, [arXiv:1111.6097 \[hep-ph\]](#).
- [12] T. Suehara and T. Tanabe, “LCFIPlus: A Framework for Jet Analysis in Linear Collider Studies”, *Nucl. Instrum. Meth.* **A808** (2016) 109–116, [arXiv:1506.08371 \[physics.ins-det\]](#).
- [13] M. Boronat, J. Fuster, I. Garcia, P. Roloff, R. Simoniello, and M. Vos, “Jet reconstruction at high-energy electron-positron colliders”, *Eur. Phys. J.* **C78** (2018) no. 2, 144, CLICDP-PUB-2017-002, [arXiv:1607.05039 \[hep-ex\]](#).

- [14] G. Moortgat-Pick, T. Abe, G. Alexander, B. Ananthanarayan, A. Babich, *et al.*, “The Role of polarized positrons and electrons in revealing fundamental interactions at the linear collider”, *Phys.Rept.* **460** (2008) 131–243, CERN-PH-TH-2005-036, DCPT-04-100, DESY-05-059, FERMILAB-PUB-05-060-T, IPPP-04-50, KEK-2005-16, PRL-TH-05-01, SHEP-05-03, SLAC-PUB-11087, [arXiv:hep-ph/0507011](#) [[hep-ph](#)].
- [15] P. Janot, “Top-quark electroweak couplings at the FCC-ee”, *JHEP* **04** (2015) 182, [arXiv:1503.01325](#) [[hep-ph](#)].
- [16] G. Durieux, A. Irlles, V. Miralles, A. Peñuelas, R. Pöschl, M. Perelló, and M. Vos, “The electro-weak couplings of the top and bottom quarks – global fit and future prospects”, IFIC/19-33, FIC/19-33, FTUV/19-0724, [arXiv:1907.10619](#) [[hep-ph](#)]. [*JHEP*12,098(2019)].

A. Details on particle separation via dE/dx

In Fig.8.6 of the IDR the separation power between different particle types is given. A useful supplementary information of this summary is the relative frequency of the different particle types. The Fig. 16 displays the normalised dE/dx spectrum for different particles in different momentum ranges for the large and the small detector model. In both cases there is a clear separation of Kaons from pions. The latter are however much more abundant. There is only a small population of protons. Figure 17 shows the dE/dx spectra for the two processes under study.

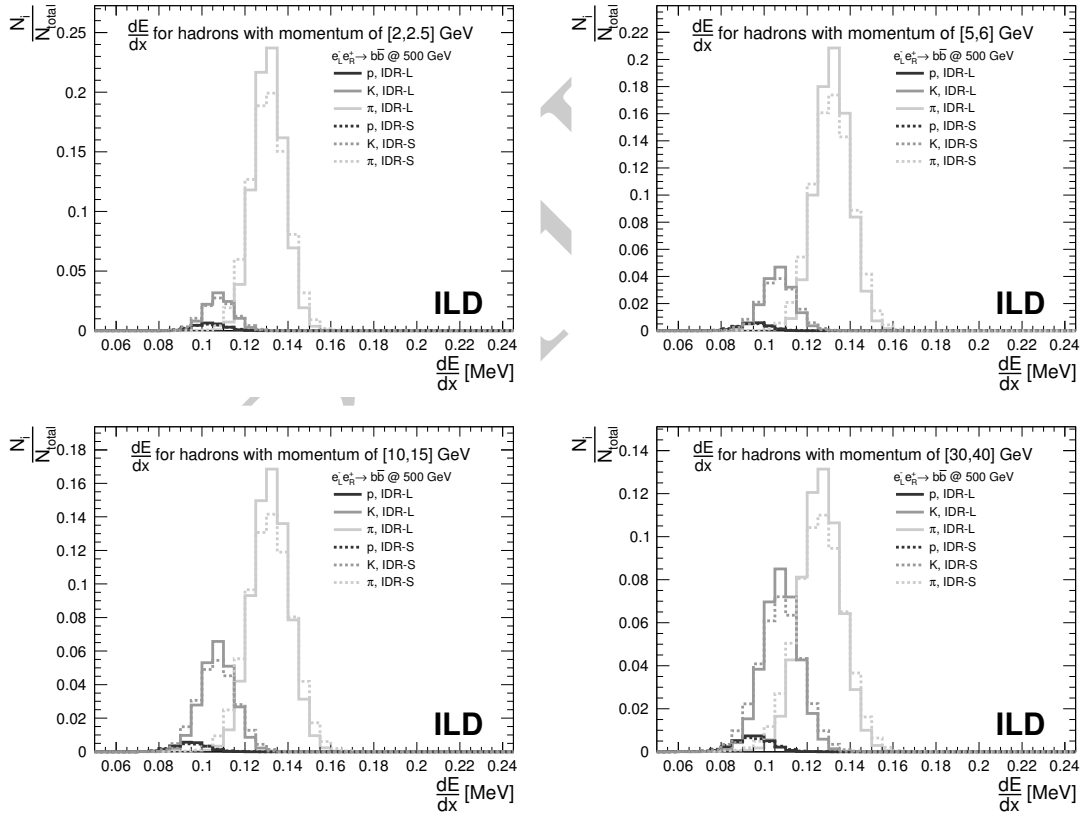


Figure 16: Projection of dE/dx for several momentum ranges. Comparison of hadron separation performance by different detector models in $b\bar{b}$ final states.

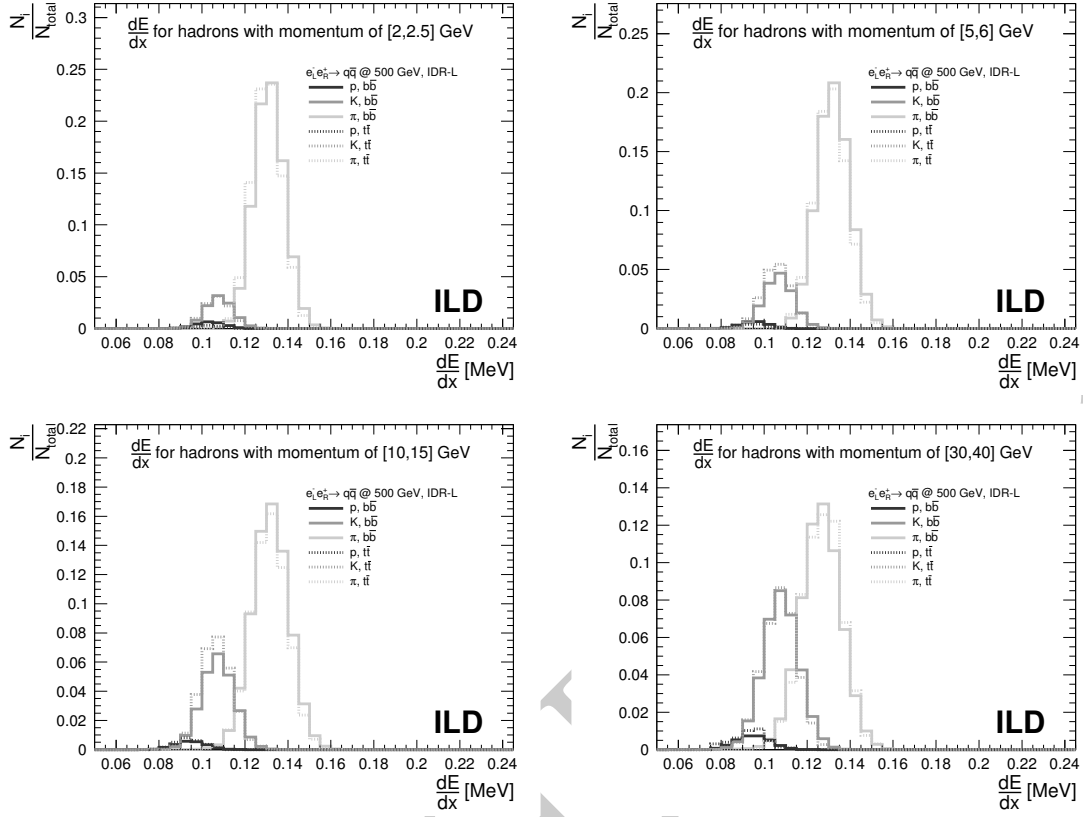


Figure 17: Projection of dE/dx for several momentum ranges. Comparison of hadron separation performance by the large model for different topologies.